FRONTIERS OF PHYSICS

RESEARCH ARTICLE
Volume 22 / Issue 2 / 025301 / 2027

Low thermal conductivity and high carrier mobility in type-II Dirac semimetal $PtTe_2$ thin films

Tianran Jiang[1], Huiping Wu[1], Shuxiang Wu[2,†], Yanqi Huang[3], Wenjie Li[3], Jing Shuai[3], Ziyu Wang[4], Tianshu Lai[1,‡], Ke Chen[1,§]

1 Guangdong Provincial Key Laboratory of Magnetoelectric Physics and Devices, State Key Laboratory of Optoelectronic Materials and Technologies, School of Physics, Sun Yat-sen University, Guangzhou 510275, China
2 School of Materials Science and Engineering, Sun Yat-sen University, Guangzhou 510275, China
3 School of Materials, Sun Yat-sen University, Shenzhen 518107, China
4 Key Laboratory of Artificial Micro-structures of Ministry of Education, School of Physics and Technology, Wuhan University, Wuhan 430072, China
Corresponding authors. E-mail: †wushx3@mail.sysu.edu.cn, ‡stslts@mail.sysu.edu.cn, §chenk35@mail.sysu.edu.cn
Received June 23, 2026; accepted August 12, 2026

© Higher Education Press 2027

ABSTRACT

High mobility is crucial for optoelectronic response and thermoelectric performance, while low thermal conductivity enhances the thermoelectric figure of merit (ZT) and reduces heat loss. $PtTe_2$, a novel two-dimension (2D) Dirac semimetal, is a promising optoelectronic and thermoelectric material. Here, we characterize 2D $PtTe_2$ films using transient thermal grating (TTG) and terahertz time-domain spectroscopy (THz-TDS). TTG reveals an extremely low thermal diffusion coefficient (~6.4×10^{-6} m^2/s), much lower than most semiconductors and metals, likely from strong phonon–phonon scattering or phonon boundary scattering, with a corresponding thermal conductivity of ~10.4 $W \cdot m^{-1} \cdot K^{-1}$. THz-TDS shows excellent electrical transport: room-temperature conductivity reaches 4.7×10^5 S/m and carrier mobility is 1870 $cm^2 \cdot V^{-1} \cdot s^{-1}$, attributed to its highly ordered crystal and Dirac band structure. The ZT is 0.002 at room temperature, comparable to reported values for 2D thermoelectric materials. Combining low thermal conductivity and high mobility, 2D $PtTe_2$ offers new opportunities for high-performance electronics and possible application in thermoelectrics.

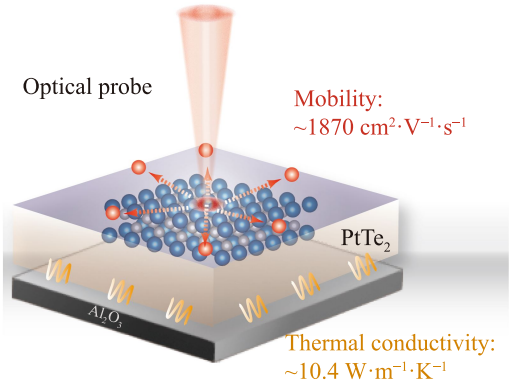

Keywords thermal conductivity, carrier mobility, transient thermal grating, terahertz time-domain spectroscopy, two-dimension Dirac semimetal

1 Introduction

Thermoelectric conversion technology serves as a crucial approach for the resource utilization of waste heat and the establishment of a low-carbon energy system [1, 2]. Its energy conversion efficiency is determined by the dimensionless figure of merit $ZT = \sigma S^2 T/\kappa$. Among them, the collaborative optimization of electrical conductivity σ (positively correlated with carrier mobility μ), Seebeck coefficient S, and thermal conductivity κ has been a core challenge for a long time [3–7]. Ultra-low thermal conductivity and high carrier mobility are two crucial parameters for thermoelectric materials. Recent advances in flexible thermoelectric films show that

https://doi.org/10.15302/frontphys.2027.025301

simultaneous efficient electrical transport and low thermal conductivity are essential for high-performance wearable flexible energy-conversion devices [4, 8, 9]. These studies also highlight the growing importance of optimizing the intrinsic electrical and thermal transport properties of novel thermoelectric materials, thereby providing guidance for rational material design and device optimization. Current strategies for reducing lattice thermal conductivity fall into three categories: (i) exploiting intrinsic phonon anharmonicity, e.g., in layered SnSe, where lattice distortion enables ultralow thermal conductivity [7]; (ii) introducing multiscale scattering centers (e.g., nanocrystalline boundaries, defects, and heterogeneous interfaces) to enhance broadband phonon scattering [3, 5, 10]; and (iii) discovering intrinsically low-κ materials with distinctive electronic structures and lattice dynamics, such as topological and Weyl semimetals [1, 11, 12]. On the other hand, carrier mobility not only governs the electrical conductivity and thermoelectric performance of materials, but also plays a pivotal role in flexible and optoelectronic energy-conversion devices. A higher carrier mobility can expedite the carrier transport process, effectively minimize the scattering loss of carriers, and consequently enhance the electrical conductivity.

In recent years, Dirac semimetals (DSMs) have introduced a novel paradigm for decoupling electrical and thermal conductivity parameters. This is due to the high carrier mobility arising from linear dispersion relations, tunable Fermi levels, and topologically protected transport characteristics [13–15]. $PtTe_2$ is a type-II Dirac semimetal with a layered CdI_2 structure and van der Waals bonding [16–18]. Its heavy Pt/Te atoms, strong phonon anharmonicity [16, 19], and layer-induced scattering suppress phonon transport [19, 20], yielding intrinsically low lattice thermal conductivity. Concurrently, its linear dispersion and topologically protected type-II Dirac bands result in low carrier effective mass and ultra-high Fermi velocity [14, 21], which enables high carrier mobility. This decouples the transport of electrons and phonons, enabling a high-mobility and low-thermal-conductivity behavior that is ideal for optoelectronics and thermoelectrics. So far, the carrier mobility reported in the Hall experiment at room temperature is less than 20 $cm^2 \cdot V^{-1} \cdot s^{-1}$ [22, 23], which is far lower than the theoretically predicted value ranging from 300 to 1200 $cm^2 \cdot V^{-1} \cdot s^{-1}$ [19, 24, 25]. This substantial discrepancy between the experimental results and the theoretical predictions can be ascribed to the errors caused by the contact measurement of non-intrinsic carrier mobility. Specifically, the fabrication of electrodes introduces significant contact resistance, interface scattering, and surface damage [26, 27]. All these factors strongly suppress the extracted mobility and mask the intrinsic transport properties. Moreover, contact measurements are susceptible to surface states, extrinsic doping, and inhomogeneous carrier accumulation near electrodes, instead of probing the intrinsic Dirac band transport of pristine $PtTe_2$. Meanwhile, theoretical predictions indicate that $PtTe_2$ has a low thermal conductivity of 0.4–10 $W \cdot m^{-1} \cdot K^{-1}$ at room temperature [16, 19, 20, 28]. These characteristics render $PtTe_2$ one of the most promising candidates for next-generation optoelectronic and thermoelectric materials at present. However, the lack of precise experimental measurements of thermal conductivity and intrinsic electrical transport properties (electrical conductivity and carrier mobility) restricts the practical assessment of $PtTe_2$ for next-generation optoelectronic, thermoelectric, and flexible energy-conversion devices. On the other hand, the optical and thermal properties of 2D $PtTe_2$ have not yet been fully understood, and there is a key gap in current research: most existing reports focus on theoretical predictions and electronic structure characterization, lacking systematic experimental characterization of thermal conductivity, electrical conductivity, and carrier mobility. To address this issue, we employed two complementary non-contact precision characterization techniques: the transient thermal grating (TTG) spectroscopy can non-destructively measure the thermal conductivity of $PtTe_2$, avoiding interface interference in contact measurements [29–35]; terahertz time-domain spectroscopy (THz-TDS) can simultaneously extract electrical conductivity and carrier mobility, reflecting the intrinsic characteristics of electron transport [36–40].

In this letter, we conducted a systematic study on the thermal conductivity, carrier transport behavior of 2D $PtTe_2$ through a synergistic combination of non-contact optical techniques: the transient thermal grating (TTG) method and terahertz time-domain spectroscopy (THz-TDS). The experimental results show that the thermal conductivity of this material at room temperature is extremely low, only 10.4 $W \cdot m^{-1} \cdot K^{-1}$. This is mainly due to the strong phonon scattering effect in its layered crystal structure, and the relatively heavy elemental mass causes the softening of the low-frequency phonon mode. Meanwhile, due to the high electron velocity endowed by Dirac fermions, the carrier mobility can reach over 1870 $cm^2 \cdot V^{-1} \cdot s^{-1}$ at room temperature, demonstrating excellent electrical transport performance. Based on this, we calculated a ZT value at room temperature close to 0.002, comparable to the typical ZT levels of conventional two-dimensional thermoelectric systems (such as 2D SnSe [41]) within the same temperature range.

2 Methods

In our experiment, $PtTe_2$ is a layered hexagonal crystal (space-group $P\bar{3}m1$, where $a = b = 4.026$ Å, $c = 5.221$ Å, $\alpha = \beta = 90°$, and $\gamma = 120°$) and demonstrates a typical CdI_2-type crystal structure. It belongs to the C_{3v}

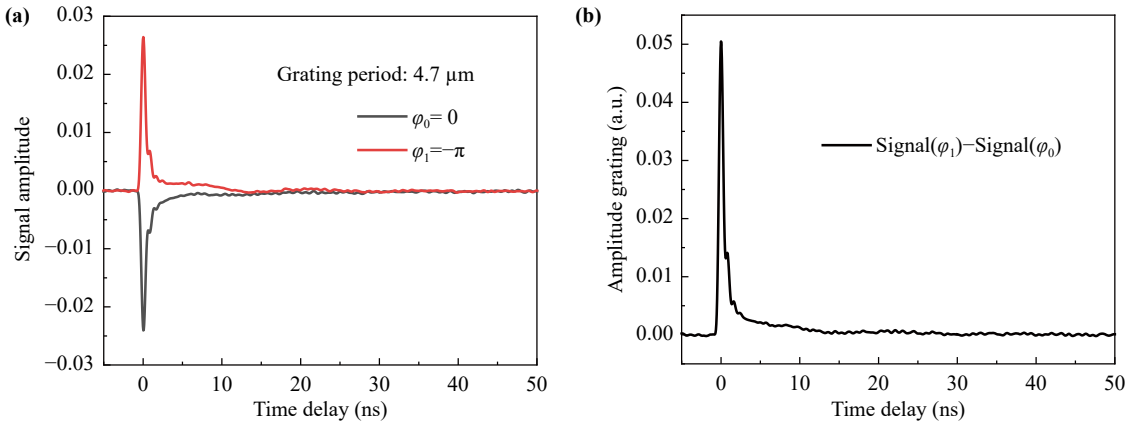

Fig. 1 **(a)** Transient grating data with a 4.7 μm grating period at two phase settings (0, –π) at 300 K. **(b)** The experimental transient grating signal traces of $PtTe_2$.

symmetry point group and has an inversion center, which is essential for stabilizing type-II Dirac nodes. Each monolayer is composed of three Te–Pt–Te atomic planes. A central Pt atom surrounded by six Te atoms forms a repeating hexagonal unit in the monolayer. In this study, wafer-scale type-II Dirac semimetal $PtTe_2$ thin films [~5.3 nm, see Fig. S1(a)] were epitaxially grown on thick Al_2O_3 substrates (hexagonal structure, $a = b = 4.758$ Å) by MBE at a rate of 0.26 nm/min. To further study the crystallinity of $PtTe_2$ films, X-ray diffraction (XRD) experiments were carried out *ex situ* at room temperature. The $PtTe_2$ epitaxial films show typical (00l) orientation with narrow full width at half-maximum (FWHM = 0.97°), suggesting high crystallinity and strict growth orientation along the c axis as shown in Fig. S1(b). The sample preparation process, along with the characterization of its homogeneity and high quality (e.g., Raman, AFM, and STEM), can be found in our previous reports [22].

The TTG system is depicted in Fig. S2(a). It comprises a femtosecond laser (515 nm, 1 kHz, ~100 fs) serving as the pump light and a 532 nm continuous laser acting as the detection light. The pump light and the detection light are focused by the achromatic lens onto the phase grating, generating ±1 order of diffractive light. Subsequently, a pair of achromatic lenses (f_1 and f_2) are used to focus ±1 order of diffractive light onto the sample surface to form a thermal grating. Gold-plated attenuation plates and phase plates are respectively introduced into the ±1-order path of the detection light. The detector receives a mixed signal of the –1-order diffracted light attenuated by gold plating and the reference light, achieving heterodyne amplification measurement (for details, see Refs. [29–35]). Heterodyne detection is a phase-sensitive technique. Its principle is to coherently superimpose the detection light with the reference light of the same wavelength and measure the combined light intensity by the detector. TTG spectroscopy measures the diffusive relaxation of a sinusoidal thermal pattern created on a thin membrane. A probe beam detects the diffracted signal, and its decay is fitted to heat diffusion theory to determine effective thermal conductivity [29–32]. Consequently, in the diffusive regime, where the grating period (Λ) is significantly larger than the mean free paths (MFPs) of thermal phonons, thermal decay follows an exponential profile $T(x,t) \propto \cos(q \cdot x)\exp(-\Gamma \cdot t)$, as predicted by Fourier heat diffusion theory. The decay rate Γ is given by $\Gamma = D \cdot q^2 = \kappa \cdot q^2 / C$, where $q = 2\pi/\Lambda$ is the grating wavevector and $D = \kappa / C$ is the thermal diffusivity. The TTG technique is employed to characterize the in-plane thermal conductivity parallel to the atomic layers. All the thermal conductivity values reported in this work correspond to the in-plane direction.

THz-TDS in the experiment was measured by the experimental setup shown in Fig. S2(b). The pump laser is provided by a Ti:sapphire oscillator (Spectra Physics) with a central wavelength of 800 nm, a pulse width of 100 fs, and a repetition rate of 80 MHz. The output beam of the oscillator is divided into two paths. One path is utilized to pump a low-temperature grown gallium arsenide photoconductive antenna (PCA) for the generation of terahertz waves. These terahertz waves are then focused and transmitted through the sample via two silicon lenses. Another path is used for terahertz electric field detection and is focused together with the terahertz wave transmitted through the sample onto another low-temperature grown GaAs PCA. The entire experimental setup is placed in an environment filled with dry air during the measurements.

3 Results and discussion

We used the TTG system to measure the transient grating heterodyne signals of $PtTe_2$ when the relative phase φ was 0 and –π, respectively. The experimental results are shown in Fig. 1(a). The experimental results clearly

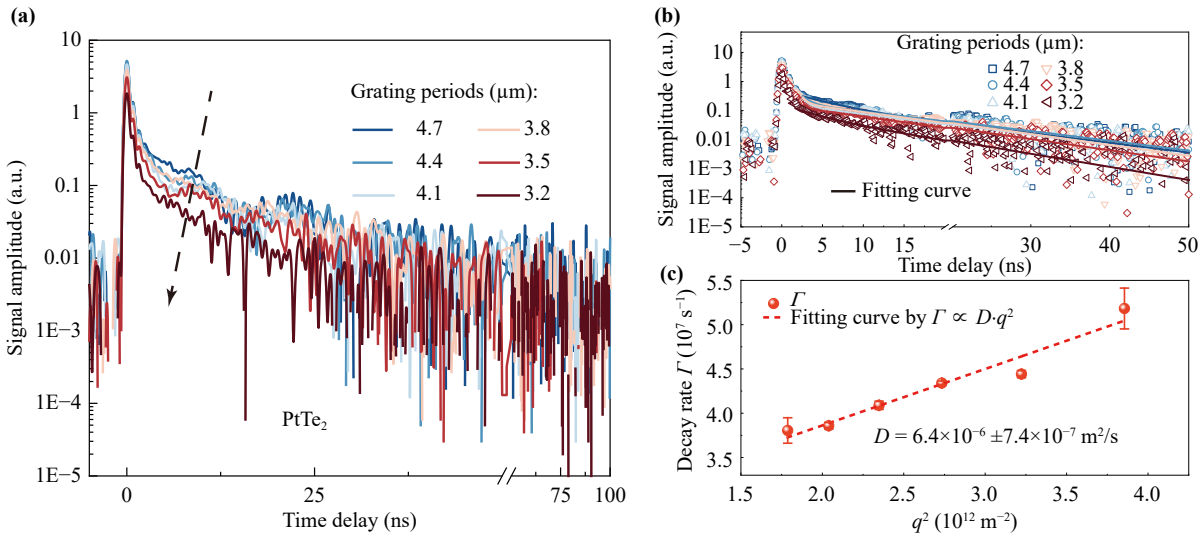

Fig. 2 **(a)** The experimental TTG traces of $PtTe_2$ with a range of grating periods at 300 K. **(b)** The solid curve with each trace is the best-fit using the Eq. (1). **(c)** Measured thermal decay rate (red circles) as a function of the grating wavevector q^2. The thermal diffusion coefficient D can be determined via fitting (indicated by the solid line).

show the attenuation of the electronic signal at short delay times and the attenuation of the thermal signal at long delay times. Meanwhile, the signs of the measured transient gratings are opposite when φ is 0 and $-\pi$. By subtracting the two grating signal curves, we can eliminate the noise and then obtain the thermal decay signal [see Fig. 1(b)]. Moreover, the following formula can be used to fit the thermal decay coefficient Γ [29–35]:

$$I(\varphi = -\pi) - I(\varphi = 0) \propto e^{-\Gamma \cdot t}, \quad (1)$$

where $\Gamma \propto D \cdot q^2$. By measuring the thermal relaxation signals corresponding to a series of grating periods, a linear fit can be made with the thermal decay rate (Γ) and the square of grating wave vector (q^2), and thus the thermal diffusion coefficient D of the grating can be obtained. Additionally, since the relationship between the thermal conductivity κ, the thermal diffusivity D, and the volumetric heat capacity C of the material can be expressed as $\kappa = D \cdot C$, the thermal conductivity κ of $PtTe_2$ can thus be determined.

We measured the thermal decay signals of the grating at different grating periods (Λ) ranging from 3.2 to 4.7 μm. The grating periods were chosen in the range of 3.2–4.7 μm, which is more than 15–120 times the room temperature phonon mean free path (MFP; ~40–200 nm) in $PtTe_2$ [28]. This ensures that $\Lambda \gg$ phonon MFP and all measurements were performed in the standard diffusive regime, where the Fourier heat diffusion model is fully valid. By observing the thermal decay curves corresponding to different grating periods in Fig. 2a, as indicated by the black arrow, we can find that the thermal decay rate increases as the grating period decreases. This is because, when the grating period is smaller, the thermal energy at the peak position of the generated transient thermal grating can be transported to the valley position more quickly and reach equilibrium. Additionally, oscillation signals can be observed on the thermal decay signals, which originate from the standing-wave patterns generated by the hot air induced by the laser in the grating region. It should be emphasized that this phonon mode is only related to the speed of sound and is not a signal generated by the $PtTe_2$ sample itself. Overall, through the measurement and analysis of thermal decay signals under different grating periods, we obtained the thermal relaxation rate Γ by means of exponential function fitting. The fitting experiment results are shown by the solid line in Fig. 2(b), and the fitting curve fits the experimental values well. We further extracted the relationship between the thermal decay rate Γ and the q^2 of the grating wave vector [see Fig. 2(c)], and then obtained through linear fitting that the thermal diffusion coefficient of the $PtTe_2$ sample D is $(6.40 \times 10^{-6} \pm 0.74) \times 10^{-6}$ m^2/s. When experimental heat capacity data for ultrathin $PtTe_2$ films is unavailable, approximating it with the volumetric heat capacity of bulk $PtTe_2$ is a common and widely accepted engineering practice in thin-film thermal property method [42, 43]. Because the crystal structure and chemical composition of the $PtTe_2$ film are consistent with those of bulk $PtTe_2$, and the lattice heat capacity is expected to exhibit much weaker thickness dependence than the thermal conductivity, this approximation is expected to introduce only a limited uncertainty into the thermal conductivity estimation [42, 44]. Based on the experimentally reported bulk heat capacity of $PtTe_2$ [45] and the bulk density, the corresponding volumetric heat capacity is estimated to be approximately 1.63×10^6 J/(K·m^3). Accordingly, the thermal conductivity for

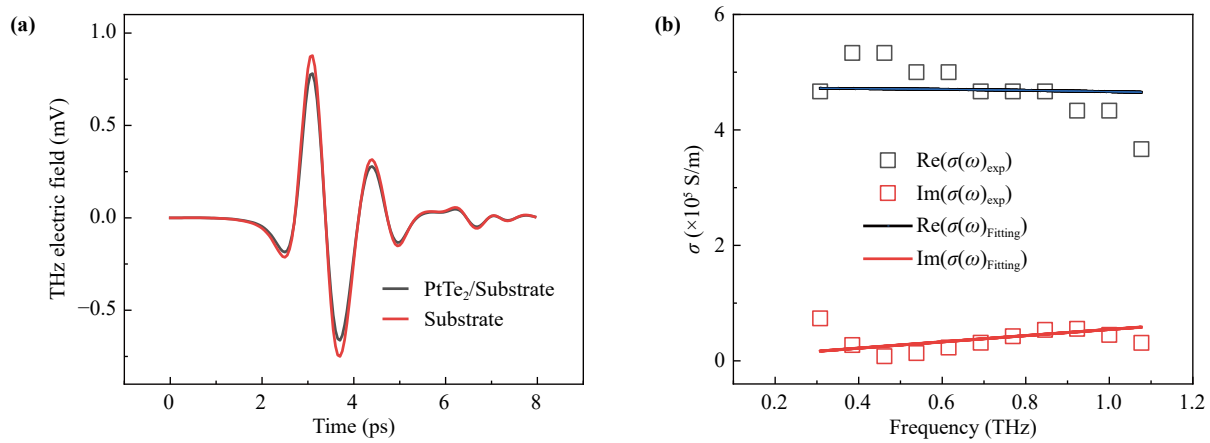

Fig. 3 **(a)** The THz electric field strength transmitted through $PtTe_2$ on the Al_2O_3 substrate (red curve) and through the bare Al_2O_3 substrate (black curve), respectively, as a function of delay time at 300 K. **(b)** Real and imaginary $\sigma(\omega)$ parts of the optical conductivity as a function of THz frequency.

ultrathin $PtTe_2$ films is calculated to be $\kappa = 10.4\ W{\cdot}m^{-1}{\cdot}K^{-1}$. The results obtained from this experiment are highly close to the theoretical prediction results [20]. The low in-plane thermal conductivity observed in the 5.3 nm $PtTe_2$ thin film results from a synergistic combination of intrinsic lattice dynamics and strong interface scattering at the $PtTe_2$-substrate boundary. This combination jointly establishes the characteristic phonon-glass thermal transport regime. The large atomic masses of Pt and Te strongly govern the phonon dispersion spectrum, giving rise to significantly reduced phonon group velocity and pronounced softening of low-frequency acoustic phonon modes [16, 19, 20]. Such mass-induced suppression of heat-carrier speed provides an intrinsic basis for low lattice thermal conductivity, since the lattice thermal conductivity scales approximately with the square of the phonon group velocity. This intrinsic suppression is further strengthened by strong intrinsic phonon-phonon anharmonic scattering [19, 20], which dominates in-plane thermal transport and promotes frequent Umklapp scattering events, substantially shortening the phonon lifetime and impeding coherent long-range phonon propagation. In addition to these intrinsic effects, the 5.3 nm $PtTe_2$ layer is in intimate contact with the Al_2O_3 substrate, introducing intensive in-plane phonon interface scattering at the heterointerface. Because the intrinsic phonon mean free path (MFP) in $PtTe_2$ (40–200 nm) is considerably longer than the film thickness [28], long-wavelength in-plane phonons cannot propagate freely without being scattered by the $PtTe_2$-substrate interface. This strong interface scattering effectively filters out the contribution of long-MFP phonons to thermal transport, providing a dominant extrinsic contribution to the reduced in-plane thermal conductivity.

To precisely determine whether a material is an ideal thermoelectric or photovoltaic material, it is essential to accurately measure its electrical conductivity or mobility. For this purpose, we analyzed the time-domain terahertz spectroscopy (THz-TDS) with and without the sample to extract the intrinsic electrical conductivity or mobility. Using THz-TDS, we measured the time-domain electric field of the THz beam transmitted through the sample ($PtTe_2$/substrate), $E_{s+sub}(t)$, and the substrate alone, $E_{sub}(t)$ [see Fig. 3(a)]. After Fourier transformation, we obtained the frequency-domain electric fields $E_{s+sub}(\omega)$ and $E_{sub}(\omega)$. The optical conductivity of $PtTe_2$ was then calculated using the Tinkham relation [36–40]:

$$\frac{E_{S+sub}(\omega)}{E_{Sub}} = \frac{1+n}{1+n+Z_0\sigma(\omega)d}, \tag{2}$$

where n is the refractive index of the substrate (~ 3.1), d is the thickness of sample, $Z_0 \approx 377$ is the impedance of the free-space, and $\sigma(\omega)$ is the complex optical conductivity with ω being the photon frequency. Figure 3b shows the spectra of the real and imaginary parts of $\sigma(\omega)$ for $PtTe_2$. We can observe that in this sample, the real and imaginary parts of $\sigma(\omega)$ show completely opposite trends of change as the frequency increases. The real part decreases with increasing frequency, while the imaginary part increases. Our previous research has clearly shown that our $PtTe_2$ belongs to an n-type Dirac semimetal [22]. Given that the energy of terahertz photons is relatively low (1 THz $\approx$ 4.13 meV), the terahertz measurement reflects the optical response of n-type $PtTe_2$ near the Fermi level. In this study, we utilized the Drude–Smith model [38, 46–48] to fit the real and imaginary parts of the experimentally-obtained optical conductivity of $PtTe_2$, which can be expressed as

$$\sigma(\omega) = \frac{\sigma_0}{1-i\omega t}\left(1+\frac{C}{1-i\omega t}\right), \tag{3}$$

where the coefficient $C = [-1, 0]$ denotes the electronic

Table 1 Carrier mobility in 2D materials by non-contact optical measurement at room temperature.

Sample	Thickness	Method	Carrier mobility ($cm^2 \cdot V^{-1} \cdot s^{-1}$)	Ref.
VP	~50 nm (thin film)	Transient absorption microscopy (TAM)	~1798	[50]
BP	~16 nm (thin film)	TAM	~10^4	[51]
$MoSe_2$	Monolayer	TAM	~480	[52]
WSe_2	Monolayer	TAM	~600	[53]
WS_2	Bilayer (thin film)	TAM	~87	[54]
MoS_2	~8.4 nm (thin film)	Raman Thermometry	~50	[55]
$PtTe_2$	~5 nm (thin film)	Terahertz time-domain spectroscopy	~1870	This work

localization factor induced by a collision between a conducting electron and a scattering center due to the backscattering mechanism with a Poisson distribution. $\sigma_0 = e^2 \cdot n_e \cdot \tau / m^*$ is the DC conductivity, n_e is the electron density in $PtTe_2$, τ is the momentum scattering time, and m^* is the effective electron mass in $PtTe_2$. During the Drude-Smith fitting procedure, the DC conductivity (σ_0), carrier scattering time (τ), and localization factor (C) were used as fitting parameters. Therefore, by programming with MATLAB and fitting the experimental results using the Drude–Smith formula [Eq. (3)], we can obtain key sample and material parameters, such as the DC conductivity $\sigma_0 = 4.7 \times 10^5$ S/m, the momentum relaxation time $\tau = 117$ fs, and the electron localization factor $C = -0.0001$. The σ_0 obtained from fitting is similar with the result measured by Hall measurement (see Fig. S3), which indicates the rationality and accuracy of the fitting. In addition, the coefficient C is close to 0, which means negligible carrier backscattering and nearly ideal free-electron transport. $PtTe_2$ is a robust type-II Dirac semimetal with a light effective mass, and it preserves its semimetallic band structure and linear Dirac dispersion down to ~3 nm thickness before transitioning to a semiconducting monolayer [23, 49]. Given that the $PtTe_2$ film thickness in this work is ~5.3 nm, well above the critical thickness for the semimetal–semiconductor transition, the electronic structure remains bulk-like, and the use of $m^* = 0.11 m_e$ is physically reasonable and consistent with the preserved Dirac band characteristics [14], where m_e represents the free electron mass. Therefore, it should be noted that once τ was obtained, the carrier mobility could be determined by $\mu = e \cdot \tau / m^* = 1870$ $cm^2 \cdot V^{-1} \cdot s^{-1}$. The high mobility is also similar with the theoretical report [19]. Notably, the carrier mobility of 2D $PtTe_2$ at room temperature is comparable to that of violet phosphorus (VP) (~ 1798 $cm^2 \cdot V^{-1} \cdot s^{-1}$) [50] and Black phosphorus (BP) (~ 10^4 $cm^2 \cdot V^{-1} \cdot s^{-1}$) [51], and it surpasses that of typical 2D TMDs such as, $MoSe_2$ (~ 480 $cm^2 \cdot V^{-1} \cdot s^{-1}$) [52], WSe_2 (~ 600 $cm^2 \cdot V^{-1} \cdot s^{-1}$) [53] WS_2 (~87 $cm^2 \cdot V^{-1} \cdot s^{-1}$) [54] and MoS_2 (~50 $cm^2 \cdot V^{-1} \cdot s^{-1}$) [55] as shown in Table 1. The high carrier mobility observed in $PtTe_2$ originates from a synergistic combination of its intrinsic topological band characteristics and excellent structural quality. First, as a type-II Dirac semimetal, this material exhibits linear band dispersion near the Fermi level, which gives rise to an ultralow effective mass and enables intrinsically fast carrier transport [14, 17]. Second, the high-quality epitaxial films, synthesized via molecular beam epitaxy (MBE), exhibit superior crystallinity as evidenced by the characterizations in Figure S1 and our previous work [22]. Such high structural integrity effectively minimizes extrinsic scattering from impurities and lattice defects, thereby preserving the intrinsic transport properties of the material. Third, carrier transport in this system is dominated by topologically protected Dirac fermions with chiral character, which inherently suppress large-angle backscattering and support long momentum relaxation times. The near-zero localization factor $C \approx 0$ obtained from Drude-Smith fitting further confirms negligible carrier backscattering and weak localization effects [39, 47], consistent with nearly ideal free-electron transport. Using the Drude conductivity relation, $\sigma_0 = e^2 \cdot n_e \cdot \tau / m^*$, we obtain a high carrier concentration of $n \approx 1.6 \times 10^{19}$ cm^{-3}, indicating the semi-metallic transport behavior of the $PtTe_2$ film. Combined with its high carrier mobility (1870 $cm^2 \cdot V^{-1} \cdot s^{-1}$), these transport properties confirm efficient electronic transport, which is consistent with the electron-crystal characteristic [14, 56].The observed coexistence of high carrier mobility and low thermal conductivity in our $PtTe_2$ films initially appears to be a physical paradox; however, such synergistic behavior has been widely reported in other systems, such as the Dirac semimetal Cd_3As_2 [57], Weyl Semimetal WTe_2 [58] and the topological insulator Bi_2Te_3 [59], where topological protection ensures efficient electronic transport while structural complexity or heavy elements impede heat flow. Our findings confirm that $PtTe_2$ is a promising candidate for high-performance thermoelectric and micro-nano electronic applications.

To quantitatively analyze the thermoelectric properties of $PtTe_2$ as a thermoelectric material, we need to calculate the value of advantage (ZT) used to describe the performance of the thermoelectric material. ZT is quantified by the formula $ZT = \sigma S^2 T / \kappa$, where S, σ, T and κ are the Seebeck coefficient, electrical conductivity, temperature and thermal conductivity, respectively. Thermal conductivity (κ) consists of electronic (κ_e) and lattice

(κ_p) contributions. The electronic thermal conductivity was estimated using the Wiedemann–Franz (WF) law, $\kappa_e = L{\cdot}\sigma{\cdot}T$ [60, 61], where L is the Lorenz number, σ is the electrical conductivity (Fig. S3), and T is the temperature. For semimetals, the Lorenz number has been reported to range from 0.98 to 2.44 × 10^{-8} W·Ω·K^{-2} [61]. Using this reported range of Lorenz numbers, the κ_e of $PtTe_2$ is estimated to be 1–3 W·m^{-1}·K^{-1}, which corresponds to approximately 10%–30% of the measured total thermal conductivity (~10.4 W·m^{-1}·K^{-1}). To date, a representative Lorenz number of L = 1.50 × 10^{-8} W·Ω·K^{-2} is frequently adopted in thermoelectric studies [7, 41]. We calculated the κ_e based on this representative value, obtaining $\kappa_e \approx 2.1$ W·m^{-1}·K^{-1}, accounting for about 20% of the total thermal conductivity. Therefore, these results consistently indicate that lattice thermal conductivity is the dominant contribution to heat transport in $PtTe_2$. Meanwhile, the κ_p of $PtTe_2$ follows a typical T^{-1} temperature dependence [19, 20], which is characteristic of Umklapp scattering in crystalline solids [4, 62]. Within the moderate-to-high temperature range, rising temperature intensifies lattice thermal vibrations and increases phonon population, remarkably enhancing intrinsic phonon-phonon scattering. This thermal transport behavior is dominated by intrinsic lattice effects rather than extrinsic scattering from impurities, defects or grain boundaries. This unique thermal property, when coupled with superior electron transport, makes $PtTe_2$ highly promising for thermoelectric applications that demand decoupled electrical and thermal transport. Consequently, we measured the Seebeck coefficient of the $PtTe_2$ film and found that it was 12 μV/K at room temperature, as shown in Fig. S4. This value is much smaller than the theoretical reported range of 233 to 324 μV/K [19, 20]. This might be due to the difference in carrier concentrations caused by n-type doping and the thickness. Finally, based on the corresponding experimental results, we calculated that the ZT value of the $PtTe_2$ thin film is approximately 0.002, which represents the intrinsic baseline performance of our unoptimized $PtTe_2$ films. Given the current limitation of a small Seebeck coefficient due to the bipolar cancellation in semimetals, where the opposing Seebeck contributions from electrons and holes partially negate each other. The significant ZT enhancement could be envisioned by selective carrier doping to break the electron–hole compensation [20]. Moreover, this ZT value of $PtTe_2$ films is lower than that of most bulk materials. Generally, the thinner the material, the smaller its ZT value is compared to that of its bulk counterpart [63, 64]. As reported in previous studies, the thermoelectric performance of $PtTe_2$ thin films is strongly thickness-dependent [65]. The power factor increases significantly with increasing film thickness due to improved carrier transport and preserved semimetallic band characteristics. Although lattice thermal conductivity may rise moderately

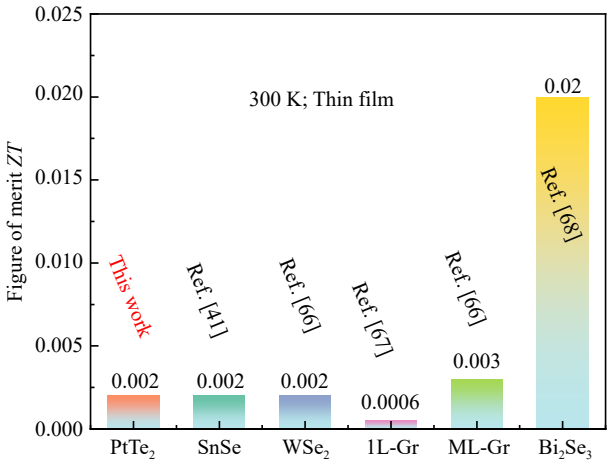

Fig. 4 A comparison of the figure of merit (ZT) of 2D $PtTe_2$ with those of other thin film materials at 300 K.

in thicker films as interface scattering weakens, the enhancement of the power factor dominates, leading to a notably improved ZT value in bulk-like $PtTe_2$. This trend is consistent with that widely observed in layered van der Waals thermoelectric material [63]. In other words, once the thickness of $PtTe_2$ increases to the level of that of a bulk material, it can be anticipated that this material will possess a considerable ZT value. Therefore, for a fair comparison, we present the experimentally measured ZT values of ultrathin $PtTe_2$ and other existing thin-film materials in Fig. 4. The ZT value at this room temperature is generally closed to or higher than that of other two-dimensional (2D) thin film materials (thickness < 10 nm) (such as SnSe [41], WSe_2 [66], monolayer graphene (1L-Gr) [67], and multilayer graphene (ML-Gr) [66]). At present, 2D Bi_2Se_3 thin film is the largest thermoelectric thin film material of ZT [68]. In particular, the fact that the ZT value of $PtTe_2$ films is comparable to that of traditional 2D SnSe thermoelectric material indicates that the bulk $PtTe_2$ could have certain thermoelectric potential as well.

4 Conclusion

We conducted research on $PtTe_2$ Dirac semi-metallic films grown by molecular beam epitaxy (MBE) using transient thermal grating technology. It was found that the thermal diffusion coefficient of this film is extremely low, approximately 6.4 × 10^{-6} m^2/s. This value is significantly lower than that of most traditional semiconductors and metals, indicating that heat spreads slowly within it. This might be due to intense phonon scattering or restricted lattice vibration conduction. Meanwhile, the thermal conductivity of the film was measured to be ~10.4 W·m^{-1}·K^{-1}, which belongs to a low thermal conductivity material. The low thermal conductivity

characteristic is conducive to maintaining the temperature gradient, thereby enhancing the thermoelectric conversion efficiency. In addition, to comprehensively evaluate the electrical properties of $PtTe_2$ films, the research team used terahertz time-domain spectroscopy technology to conduct non-contact measurements. The measurement results show that the electrical conductivity of this material at room temperature reaches the order of 4.7×10^5 S/m, and the carrier mobility is as high as 1870 $cm^2 \cdot V^{-1} \cdot s^{-1}$, which fully demonstrates its excellent carrier transport ability. These results reflect that $PtTe_2$ has the characteristics of a highly ordered crystal structure, a low defect density, and a Dirac band structure. These properties are conducive to the rapid diffusion of electrons in the material. In short, our study confirms that the large-area $PtTe_2$ Dirac semimetal is a highly promising candidate for optoelectronic devices.

Declarations The authors declare that they have no known competing financial interests or personal relationships that could have appeared to influence the work reported in this paper.

Data availability The datasets generated during and/or analyzed during the current study are available from the corresponding author on reasonable request.

Electronic supplementary materials The online version contains supplementary material available at https://doi.org/10.15302/frontphys.2027.025301.

Acknowledgements This work was supported by the National Key Research and Development Program of China (No. 2023YFB4603801), the National Natural Science Foundation of China (Grant Nos. 52176173, 21FAA02809, and 12304386), the Guangdong Innovative and Entrepreneurial Research Team Program (Grant No. 2021ZT09L227), the Basic and Applied Basic Research Foundation of Guangdong Province (Grant Nos. 2024A1515010409 and 2023B1515040023), and the Natural Science Foundation of Guangdong Province (Grant Nos. 2024A1515010409). The experiments reported were partially conducted at the Guangdong Provincial Key Laboratory of Magnetoelectric Physics and Devices (No. 2026B1212170049).

References

1. J. He and T. M. Tritt, Advances in thermoelectric materials research: Looking back and moving forward, *Science* 357(6358), eaak9997 (2017)
2. Z. G. Chen, X. Shi, L. D. Zhao, and J. Zou, High-performance SnSe thermoelectric materials: Progress and future challenge, *Prog. Mater. Sci.* 97, 283 (2018)
3. L. D. Zhao, G. Tan, S. Hao, J. He, Y. Pei, H. Chi, H. Wang, S. Gong, H. Xu, V. P. Dravid, C. Uher, G. J. Snyder, C. Wolverton, and M. G. Kanatzidis, Ultrahigh power factor and thermoelectric performance in hole-doped single-crystal SnSe, *Science* 351(6269), 141 (2016)
4. B. Qin, M. G. Kanatzidis, and L. D. Zhao, The development and impact of tin selenide on thermoelectrics, *Science* 386(6719), eadp2444 (2024)
5. B. Jia, D. Wu, L. Xie, W. Wang, T. Yu, S. Li, Y. Wang, Y. Xu, B. Jiang, Z. Chen, Y. Weng, and J. He, Pseudo-nanostructure and trapped-hole release induce high thermoelectric performance in PbTe, *Science* 384(6691), 81 (2024)
6. W. Zhao, Z. Liu, Z. Sun, Q. Zhang, P. Wei, X. Mu, H. Zhou, C. Li, S. Ma, D. He, P. Ji, W. Zhu, X. Nie, X. Su, X. Tang, B. Shen, X. Dong, J. Yang, Y. Liu, and J. Shi, Superparamagnetic enhancement of thermoelectric performance, *Nature* 549(7671), 247 (2017)
7. L. D. Zhao, S. H. Lo, Y. Zhang, H. Sun, G. Tan, C. Uher, C. Wolverton, V. P. Dravid, and M. G. Kanatzidis, Ultralow thermal conductivity and high thermoelectric Figure of merit in SnSe crystals, *Nature* 508(7496), 373 (2014)
8. L. C. Yin, X. Lu, W. D. Liu, and J. W. Hou, Two-step annealing process drives high thermoelectric performance of n-type Bi_2Te_3 flexible films, *Respons. Mater.* 4(3), e70056 (2026)
9. Y. M. Liu, X. L. Shi, T. Wu, H. Wu, Y. Mao, T. Cao, D. Z. Wang, W. D. Liu, M. Li, Q. Liu, and Z. G. Chen, Boosting thermoelectric performance of single-walled carbon nanotubes-based films through rational triple treatments, *Nat. Commun.* 15(1), 3426 (2024)
10. J. Mao, Z. Liu, J. Zhou, H. Zhu, Q. Zhang, G. Chen, and Z. Ren, Advances in thermoelectrics, *Adv. Phys.* 67(2), 69 (2018)
11. Y. Pan, B. He, T. Helm, D. Chen, W. Schnelle, and C. Felser, Ultrahigh transverse thermoelectric power factor in flexible Weyl semimetal WTe_2, *Nat. Commun.* 13(1), 3909 (2022)
12. R. Cheng, H. Ge, S. Huang, S. Xie, Q. Tong, H. Sang, F. Yan, L. Zhu, R. Wang, Y. Liu, M. Hong, C. Uher, Q. Zhang, W. Liu, and X. Tang, Unraveling electronic origins for boosting thermoelectric performance of p-type $(Bi, Sb)_2Te_3$, *Sci. Adv.* 10(21), eadn9959 (2024)
13. M. T. Edmonds, J. L. Collins, J. Hellerstedt, I. Yudhistira, L. C. Gomes, J. N. B. Rodrigues, S. Adam, and M. S. Fuhrer, Spatial charge inhomogeneity and defect states in topological Dirac semimetal thin films of Na_3Bi, *Sci. Adv.* 3(12), eaao6661 (2017)
14. O. Pavlosiuk and D. Kaczorowski, Galvanomagnetic properties of the putative type-II Dirac semimetal $PtTe_2$, *Sci. Rep.* 8(1), 11297 (2018)
15. T. Liang, Q. Gibson, M. N. Ali, M. Liu, R. J. Cava, and N. P. Ong, Ultrahigh mobility and giant magnetoresistance in the Dirac semimetal Cd_3As_2, *Nat. Mater.* 14(3), 280 (2015)
16. J. Zhang, Y. Xie, Y. Hu, and H. Shao, Remarkable intrinsic ZT in the 2D PtX_2 (X = O, S, Se, Te) monolayers at room temperature, *Appl. Surf. Sci.* 532, 147387 (2020)
17. M. Yan, H. Huang, K. Zhang, E. Wang, W. Yao, K. Deng, G. Wan, H. Zhang, M. Arita, H. Yang, Z. Sun, H. Yao, Y. Wu, S. Fan, W. Duan, and S. Zhou, Lorentz-violating type-II Dirac fermions in transition metal dichalcogenide $PtTe_2$, *Nat. Commun.* 8(1), 257 (2017)
18. A. Politano, G. Chiarello, B. Ghosh, K. Sadhukhan, C. N. Kuo, C. S. Lue, V. Pellegrini, and A. Agarwal, 3D Dirac plasmons in the type-II Dirac semimetal $PtTe_2$,

Phys. Rev. Lett. 121(8), 086804 (2018)
19. Y. Wang, N. D. Chen, C. Yang, Z. Y. Zeng, C. E. Hu, and X. R. Chen, Thermoelectric transport properties of two-dimensional materials XTe_2 (X = Pd, Pt) via first-principles calculations, *Acta Phys. Sin.* 70(11), 116301 (2021)
20. W. L. Tao, Y. Q. Zhao, Z. Y. Zeng, X. R. Chen, and H. Y. Geng, Anisotropic thermoelectric materials: Pentagonal PtM_2 (M = S, Se, Te), *ACS Appl. Mater. Interfaces* 13(7), 8700 (2021)
21. S. R. K. Amit, R. K. Singh, N. Wadehra, S. Chakraverty, and Y. Singh, Type-II Dirac semimetal candidates ATe_2 (A=Pt, Pd): A de Haas–van Alphen study, *Phys. Rev. Mater.* 2(11), 114202 (2018)
22. M. Y. Chen, T. R. Jiang, J. L. Wang, Z. He, H. Wu, J. Li, X. Guo, W. Li, P. Liu, H. Chen, P. Yu, X. Chen, I. K. Sou, T. Lai, S. Li, K. Chen, and S. Wu, Giant photogalvanic effect-induced terahertz wave emission in wafer-scale type-II Dirac semimetal PtTe, *ACS Appl. Mater. Interfaces* 17(2), 4137 (2025)
23. H. Ma, P. Chen, B. Li, J. Li, R. Ai, Z. Zhang, G. Sun, K. Yao, Z. Lin, B. Zhao, R. Wu, X. Tang, X. Duan, and X. Duan, Thickness-tunable synthesis of ultrathin type-II dirac semimetal $PtTe_2$ single crystals and their thickness-dependent electronic properties, *Nano Lett.* 18(6), 3523 (2018)
24. W. Zhang, Z. Huang, W. Zhang, and Y. Li, Two-dimensional semiconductors with possible high room temperature mobility, *Nano Res.* 7(12), 1731 (2014)
25. C. Zhang, R. Wang, H. Mishra, and Y. Liu, Two-dimensional semiconductors with high intrinsic carrier mobility at room temperature, *Phys. Rev. Lett.* 130(8), 087001 (2023)
26. S. Yue, F. Tian, X. Sui, M. Mohebinia, X. Wu, T. Tong, Z. Wang, B. Wu, Q. Zhang, Z. Ren, J. Bao, and X. Liu, High ambipolar mobility in cubic boron arsenide revealed by transient reflectivity microscopy, *Science* 377(6604), 433 (2022)
27. K. Sun, W. Xia, C. Wang, P. Suo, Y. Zou, J. Peng, W. Wang, X. Lin, Z. Jin, Y. Guo, and G. Ma, Highly intrinsic carrier mobility in tin diselenide crystal accessed with ultrafast terahertz spectroscopy, *Opt. Express* 32(10), 17657 (2024)
28. H. Qin, G. Zhang, K. Ren, and Q. X. Pei, Thermal conductivities of PtX_2 (X = S, Se, and Te) monolayers: A comprehensive molecular dynamics study, *J. Phys. Chem. C* 127(17), 8411 (2023)
29. U. Choudhry, T. Kim, M. Adams, J. Ranasinghe, R. Yang, and B. Liao, Characterizing microscale energy transport in materials with transient grating spectroscopy, *J. Appl. Phys.* 130(23), 231101 (2021)
30. C. A. Dennett and M. P. Short, Thermal diffusivity determination using heterodyne phase insensitive transient grating spectroscopy, *J. Appl. Phys.* 123(21), 215109 (2018)
31. J. A. Johnson, A. A. Maznev, M. T. Bulsara, E. A. Fitzgerald, T. C. Harman, S. Calawa, C. J. Vineis, G. Turner, and K. A. Nelson, Phase-controlled, heterodyne laser-induced transient grating measurements of thermal transport properties in opaque material, *J. Appl. Phys.* 111(2), 023503 (2012)
32. A. Založnik, M. J. Simmonds, B. D. Schwendeman, N. Boechler, M. J. Baldwin, and G. R. Tynan, Analytical model for laser-induced transient grating measurements of thermal diffusivity in non-opaque materials, *J. Appl. Phys.* 135(12), 125108 (2024)
33. K. Chen, B. Song, N. K. Ravichandran, Q. Zheng, X. Chen, H. Lee, H. Sun, S. Li, G. A. G. Udalamatta Gamage, F. Tian, Z. Ding, Q. Song, A. Rai, H. Wu, P. Koirala, A. J. Schmidt, K. Watanabe, B. Lv, Z. Ren, L. Shi, D. G. Cahill, T. Taniguchi, D. Broido, and G. Chen, Ultrahigh thermal conductivity in isotope-enriched cubic boron nitride, *Science* 367(6477), 555 (2020)
34. Z. Ding, K. Chen, B. Song, J. Shin, A. A. Maznev, K. A. Nelson, and G. Chen, Observation of second sound in graphite over 200 K, *Nat. Commun.* 13(1), 285 (2022)
35. S. Huberman, R. A. Duncan, K. Chen, B. Song, V. Chiloyan, Z. Ding, A. A. Maznev, G. Chen, and K. A. Nelson, Observation of second sound in graphite at temperatures above 100 K, *Science* 364(6438), 375 (2019)
36. P. R. Whelan, Q. Shen, D. Luo, M. Wang, R. S. Ruoff, P. U. Jepsen, P. Bøggild, and B. Zhou, Reference-free THz-TDS conductivity analysis of thin conducting films, *Opt. Express* 28(20), 28819 (2020)
37. T. I. Jeon and D. Grischkowsky, Characterization of optically dense, doped semiconductors by reflection THz time domain spectroscopy, *Appl. Phys. Lett.* 72(23), 3032 (1998)
38. M. Bilal, W. Xu, C. Wang, H. Wen, X. Zhao, D. Song, and L. Ding, Optoelectronic properties of monolayer hexagonal boron nitride on different substrates measured by terahertz time-domain spectroscopy, *Nanomaterials (Basel)* 10(4), 762 (2020)
39. C. Wang, W. Xu, H. Mei, H. Qin, X. Zhao, C. Zhang, H. Yuan, J. Zhang, Y. Xu, P. Li, and M. Li, Substrate-induced electronic localization in monolayer MoS_2 measured via terahertz spectroscopy, *Opt. Lett.* 44(17), 4139 (2019)
40. J. H. Strait, P. Nene, and F. Rana, High intrinsic mobility and ultrafast carrier dynamics in multilayer metal-dichalcogenideMoS_2, *Phys. Rev. B* 90(24), 245402 (2014)
41. M. R. Burton, T. Liu, J. McGettrick, S. Mehraban, J. Baker, A. Pockett, T. Watson, O. Fenwick, and M. J. Carnie, Thin film tin selenide (SnSe) thermoelectric generators exhibiting ultralow thermal conductivity, *Adv. Mater.* 30(31), 1801357 (2018)
42. J. Liu, J. Zhu, M. Tian, X. Gu, A. Schmidt, and R. Yang, Simultaneous measurement of thermal conductivity and heat capacity of bulk and thin film materials using frequency-dependent transient thermoreflectance method, *Rev. Sci. Instrum.* 84(3), 034902 (2013)
43. P. E. Hopkins, J. R. Serrano, L. M. Phinney, S. P. Kearney, T. W. Grasser, and C. T. Harris, Criteria for cross-plane dominated thermal transport in multilayer thin film systems during modulated laser heating, *J. Heat Transfer* 132(8), 081302 (2010)
44. P. Jiang, X. Qian, and R. Yang, Tutorial: Time-domain thermoreflectance (TDTR) for thermal property charac-

terization of bulk and thin film materials, *J. Appl. Phys.* 124(16), 161103 (2018)
45. D. A. Chareev, A. V. Tyurin, N. A. Polotnyanko, and P. V. Chareeva, Synthesis and low-temperature thermodynamic functions of platinum ditelluride, *Inorg. Mater.* 59(8), 825 (2023)
46. J. Yang, S. Jiang, J. Xie, H. Jiang, S. Xu, K. Zhang, Y. Shi, Y. Zhang, Z. Zeng, G. Fang, T. Wang, and F. Su, Identifying the intermediate free-carrier dynamics across the charge separation in monolayer $MoS_2/ReSe_2$ heterostructures, *ACS Nano* 15(10), 16760 (2021)
47. W. Zhang, K. Sun, P. Suo, X. Yan, X. Lin, Z. Jin, and G. Ma, Ultrafast photocarrier dynamics in vertically aligned SnS_2 nanoflakes probing with transient terahertz spectroscopy, *Nanomaterials (Basel)* 13(1), 5 (2022)
48. T. Handa, M. Holbrook, N. Olsen, L. N. Holtzman, L. Huber, H. I. Wang, M. Bonn, K. Barmak, J. C. Hone, A. N. Pasupathy, and X. Zhu, Spontaneous exciton dissociation in transition metal dichalcogenide monolayers, *Sci. Adv.* 10(5), eadj4060 (2024)
49. L. Han, Y. Zou, Q. Zeng, X. Guan, B. Jia, Y. Gao, G. Liu, and L. Wu, Strong interlayer interaction in two-dimensional layered $PtTe_2$, *J. Solid State Chem.* 305, 122657 (2022)
50. X. K. Feng, J. Y. Tan, X. Q. Cao, P. Shao, T. Han, Y. Wu, D. Lu, Y. Zhou, X. Li, Y. Huang, and X. Xu, High ambipolar mobility and long-range carrier transport in violet phosphorus nanosheet, *Nano Lett.* 24(33), 10348 (2024)
51. J. He, D. He, Y. Wang, Q. Cui, M. Z. Bellus, H. Y. Chiu, and H. Zhao, Exceptional and anisotropic transport properties of photocarriers in black phosphorus, *ACS Nano* 9(6), 6436 (2015)
52. N. Kumar, Q. Cui, F. Ceballos, D. He, Y. Wang, and H. Zhao, Exciton diffusion in monolayer and bulk $MoSe_2$, *Nanoscale* 6(9), 4915 (2014)
53. Q. Cui, F. Ceballos, N. Kumar, and H. Zhao, Transient absorption microscopy of monolayer and bulk WSe_2, *ACS Nano* 8(3), 2970 (2014)
54. Y. Zhong, S. Yue, J. Liang, L. Yuan, Y. Xia, Y. Tian, Y. Zheng, Y. Zhang, W. Du, D. Li, S. Chen, A. Pan, and X. Liu, Twist angle-dependent exciton mobility in WS_2 bilayers, *Nano Lett.* 25(13), 5274 (2025)
55. P. Yuan, J. Liu, R. Wang, and X. Wang, The hot carrier diffusion coefficient of sub-10 nm virgin MoS_2: uncovered by non-contact optical probing, *Nanoscale* 9(20), 6808 (2017)
56. G. J. Snyder and E. S. Toberer, Complex thermoelectric materials, *Nat. Mater.* 7(2), 105 (2008)
57. H. Wang, X. Luo, W. Chen, N. Wang, B. Lei, F. Meng, C. Shang, L. Ma, T. Wu, X. Dai, Z. Wang, and X. Chen, Magnetic-field enhanced high-thermoelectric performance in topological Dirac semimetal Cd_3As_2 crystal, *Sci. Bull. (Beijing)* 63(7), 411 (2018)
58. W. Tian, W. Yu, X. Liu, Y. Wang, and J. Shi, A review of the characteristics, synthesis, and thermodynamics of type-II Weyl semimetal WTe_2, *Materials (Basel)* 11(7), 1185 (2018)
59. Q. Jin, S. Jiang, Y. Zhao, D. Wang, J. Qiu, D. M. Tang, J. Tan, D. M. Sun, P. X. Hou, X. Q. Chen, K. Tai, N. Gao, C. Liu, H. M. Cheng, and X. Jiang, Flexible layer-structured Bi_2Te_3 thermoelectric on a carbon nanotube scaffold, *Nat. Mater.* 18(1), 62 (2019)
60. Y. Huang, J. Spiece, T. Parker, A. Lee, Y. Gogotsi, and P. Gehring, Violation of the Wiedemann–Franz law and ultralow thermal conductivity of $Ti_3C_2T_x$ MXene, *ACS Nano* 18(47), 32491 (2024)
61. W. Xie, F. Yang, L. Xu, X. Li, Z. Zhu, and K. Behnia, Purity-dependent Lorenz number, electron hydrodynamics and electron-phonon coupling in WTe_2, *Sci. China Phys. Mech. Astron.* 67(8), 287014 (2024)
62. A. Bhui, S. Biswas, S. Paul, S. Das, A. Ghosh, D. Swain, T. K. Maji, S. K. Pati, and K. Biswas, Atomic off-centering driven phonon-glass electron-crystal-like thermoelectric transport in entropy-stabilized quinary telluride, *J. Am. Chem. Soc.* 147(32), 29542 (2025)
63. W. Yu, N. Van Toan, Y. J. Li, Z. Wang, T. Ono, and R. Wang, Morphological analysis and properties evaluation of electrodeposited thick BiSbTe films with cooperative interactions among multiple additives, *J. Electrochem. Soc.* 168(2), 022505 (2021)
64. D. D. Yang, H. Tong, L. J. Zhou, and X. S. Miao, Effects of thickness and temperature on thermoelectric properties of Bi_2Te_3-based thin films, *Chin. Phys. Lett.* 34(12), 127301 (2017)
65. S. H. Kim, M. S. Kang, J. W. Choi, J. M. Cho, Y. H. Kim, N. W. Park, G. S. Kim, and S. K. Lee, Thickness-dependent in-plane thermoelectric properties of $PtTe_2$ with n-type conduction, *J. Phys. Chem. C* 127(3), 1673 (2023)
66. M. Rahimi, K. Sobnath, F. Mallet, P. Lafarge, C. Barraud, W. Daney de Marcillac, D. Fournier, and M. L. Della Rocca, Complete determination of thermoelectric and thermal properties of supported few-layer two-dimensional materials, *Phys. Rev. Appl.* 19(3), 034075 (2023)
67. M. Choi, T. G. Novak, J. Byen, H. Lee, J. Baek, S. Hong, K. Kim, J. Song, H. Shin, and S. Jeon, Significantly enhanced thermoelectric performance of graphene through atomic-scale defect engineering via mobile hot-wire chemical vapor deposition systems, *ACS Appl. Mater. Interfaces* 13(20), 24304 (2021)
68. J. Andzane, A. Felsharuk, A. Sarakovskis, U. Malinovskis, E. Kauranens, M. Bechelany, K. A. Niherysh, I. V. Komissarov, and D. Erts, Thickness-dependent properties of ultrathin bismuth and antimony chalcogenide films formed by physical vapor deposition and their application in thermoelectric generators, *Mater. Today Energy* 19, 100587 (2021)